Materials Horizons

ROYAL SOCIETY OF CHEMISTRY

COMMUNICATION

View Article Online
View Journal

Cite this: DOI: 10.1039/d6mh00119j

Received 21st January 2026,
Accepted 19th March 2026

DOI: 10.1039/d6mh00119j

rsc.li/materials-horizons

Concurrent selective laser sintering and graphitization of polyimide microparticles into functional and flexible 3D structures for energy storage and sensing

Muxuan Yang,[ab] Jinyu Bu,[b] Pushkar N. Dalal,[a] Leyi Deng,[a] Mingcheng Liu,[b] Laura Brady[c] and Weinan Xu *[ab]

Selective laser sintering (SLS) is an emerging technology for the fabrication of 3D complex polymeric structures by sintering polymer microparticles. But its application is constrained by the limited material selection and functionality of the polymer microparticles. To address this major challenge, here we creatively integrate SLS with polyimide and its hybrid microparticles, so that concurrent SLS and graphitization enables the precise fabrication of 2D/3D patterned and conductive graphene structures. By chemically modifying the polyimide microparticles with metal salt precursors, 3D graphene-FeO_x hybrid structures with precisely controlled geometry can be achieved after SLS. Furthermore, by sequential SLS with two types of polymer microparticles, such as thermoplastic polyurethane and polyimide, 3D soft and flexible structures with a conductive graphene coating can be conveniently fabricated. We also demonstrate promising applications of such 2D/3D hybrid structures in energy storage and strain sensors. The electrochemical capacitance or electrical responses can be widely tuned by controlling the SLS fabrication process and parameters. Our approach provides a new and versatile platform for the advanced manufacturing of soft and conductive 2D/3D structures with promising applications in energy and electronics.

New concepts

This work represents a new and versatile approach for the creation of 3D hierarchical structures with high conductivity and mechanical flexibility. Our approach is based on the synergistic integration of laser-induced graphitization and selective laser sintering (SLS) 3D printing. It is discovered that when polyimide microparticles were used as the precursors for selective laser sintering, concurrent particle sintering and graphitization processes occur, which enable the precise fabrication of 2D/3D patterned and conductive graphene structures. Moreover, through sequential SLS with two types of polymer microparticles, such as polyimide and thermoplastic polyurethane, 3D soft and flexible structures with a conductive graphene coating can be conveniently fabricated. Our work is distinct from other research on laser-induced graphene or SLS printing by integrating and combining the advantages of the two seemingly distant fields. The demonstrated capability to fabricate 3D precise hierarchical graphene and its hybrid structures from polymer particle precursors will pave the way for its broad applications in energy and electronics.

1. Introduction

The advanced manufacturing of 3D soft, flexible, and conductive structures is critically important for many fields, including flexible electronics, sensors, and energy conversion and storage.[1–3] However, it is still challenging to simultaneously achieve high processability, mechanical flexibility, and high electrical conductivity, due to the limitation of the intrinsic physical properties of soft materials. Although it is feasible to combine such properties at the material level by integrating conductive nanofillers with soft polymeric matrices,[4–7] many of those nanocomposite systems are not compatible with state-of-the-art additive manufacturing or 3D printing technologies.[8]

Among the widely used 3D printing technologies for soft materials,[9–13] selective laser sintering (SLS) has emerged as one of the most promising ones for many industrial applications.[5,14] Its unique advantages include the ability to fabricate 3D complex structures without support, highly isotropic properties of the printed parts, and batch production of multiple parts in one printing.[15–17] To be compatible with SLS 3D printing, the polymer particles need to have a combination of properties in the targeted ranges,[18,19] which include the intrinsic thermal, rheological, and optical properties, as well as the particle shape, size, and polydispersity.[14] Because of this, there is very limited selection of available polymer microparticles,[20–22] with polyamide (Nylon 12 and 11) makes

[a] Department of Materials Science and Engineering, University of Tennessee, Knoxville, TN 37996, USA. E-mail: wxu@utk.edu
[b] School of Polymer Science and Polymer Engineering, The University of Akron, OH 44325, USA
[c] Department of Chemical and Biomolecular Engineering, University of Tennessee, Knoxville, TN 37996, USA

up more than 95% of the market, and a few other polymers such as thermoplastic polyurethane and polyethylene being studied.[23,24]

Another major limitation of conventional SLS is the fabricated 3D polymer structures generally lack functionalities due to the intrinsic limit in electrical, thermal, and optical properties of polymers.[25,26] It is highly desirable if SLS printability and high electrical or thermal conductivity can be achieved at the same time. One potential approach to realize such objective is by designing polymer microparticles that can be converted into conductive structures during the laser irradiation of the SLS process. This has never been achieved in 3D SLS printing. In conventional 2D format, this process has been achieved, especially through the laser-induced graphene (LIG) approach.[27]

Conventional LIG is generally conducted through a laser photothermal process that converts certain types of thin polymer films (such as polyimide or PI, polyether ether ketone, polyethylenimine, and biopolymers) into porous graphene,[28–32] and has already been applied in various applications including electronics,[33–35] energy storage,[36–38] and sensing.[39–41] Compared with other methods for graphene production that usually requires high temperatures and harsh chemical treatments, LIG is more efficient and convenient.[42–44] The resulted graphene structures can have high electrical conductivity, large surface area, and tunable morphology.[45,46] The highly localized graphene generation upon laser irradiation also enables facile 2D patterning without the need for lithography-based patterning process.[47]

Despite the significant progress and advantages of conventional LIG process, there are two major limitations. The first one is the difficulty in fabricating macroscopic 3D structure beyond 2D films.[48–50] The second one is the requirement of additional transfer steps after LIG to the target substrates for many applications.[51] For instance, PI film is the most commonly used precursors for LIG, and the resulting LIG is inherently 2D as the top layer of the supporting PI film. Also, in order to transfer the LIG from the precursor film onto the target substrate, additional polymer casting and peeling off step is generally used.[52,53] Such a transfer step is time consuming and can lead to deterioration or damage to the LIG.

In this study, we aim to address those important limitations of both SLS 3D printing and conventional laser-induced graphene process by innovatively integrating their unique advantages. PI microparticles are studied as the new material platform for SLS 3D printing, which also transform into graphene under suitable laser conditions. Thus, the concurrent SLS and laser-induced graphitization enables the fabrication of 3D graphene structures with precisely controlled and customizable geometry and thickness. Moreover, by sequential SLS printing of PI and TPU microparticles, we demonstrate a versatile and efficient approach for the fabrication of 3D flexible structures with conductive graphene layer intimately integrated on their surface. Such unique capabilities also enable the fabrication of flexible energy storage and sensing devices with high performance and stability.

2. Results and discussion

2.1. SLS with PI microparticles for 3D porous graphene creation

The process of fabricating 3D graphene and its hybrid 2D/3D structures based on SLS printing with PI microparticles is shown in Fig. 1a. During conventional SLS 3D printing process, the laser beam scans the polymer powder bed along the pattern of each cross-section of the digital 3D model. After one layer is complete, the printing platform lowers and another layer is printed on top of the previous layer. This process continues until the whole 3D structure is completed. At the microscopic level, the neighboring polymer microparticles are (partially) melted by the laser beam, and then coalesce to form a continuous layer. In our system, the distinct feature is that the polyimide microparticles have very high glass transition and melting temperatures compared with conventional polymer powders such as Nylon. More importantly, polyimide undergoes graphitization under strong laser irradiation.[54] Therefore, unlike the conventional SLS process, here, the PI microparticles experience two processes: melting/coalescence and carbonization/graphitization, the extent of which depends on the laser intensity and local temperature. As a result of the concurrent SLS and graphitization, 3D graphene structures with well-defined geometry can be fabricated.

SEM image of the PI microparticles (Fig. 1b) shows that their sizes are in the range of 5 to 30 μm, which falls in the suitable range for SLS 3D printing. DSC characterization (Fig. S1) shows that the T_g of PI is about 250 °C, and the T_m is about 384 °C. The crystallization peak during cooling cycle occurs at 320 °C. The unique structural transformation of PI microparticles during SLS process into graphene provides a versatile and powerful platform for the advanced manufacturing of customizable 2D/3D structures with high conductivity and hierarchical morphologies. We also characterized the flowability of the PI microparticles, which is directly related to how easy it is to spread microparticles into a uniform layer on the printing platform. The commonly used parameter is Hausner ratio, which is defined by the ratio of tapped density and bulk density of the powders. Particles with Hausner ratio smaller than 1.25 are generally considered free-flowing and suitable for SLS printing.[23] In our study (Table S1), the PI and its hybrid microparticles show Hausner ratio in the range of 1.21 to 1.25, which is beneficial for their SLS printing.

We investigated two different fabrication strategies based on SLS with PI microparticles. In the first approach, PI microparticles are used as the sole powder source, after the SLS process, free-standing 3D graphene structures can be generated that are mechanically flexible (Fig. 1c). Moreover, an arbitrary substrate, such as polymer, glass, or steel can be placed under the PI microparticles during the SLS process, which will result in patterned 3D graphene on those target substrates. Fig. 1d shows the 3D graphene in the pattern of a university seal on a piece of PDMS substrate fabricated by the SLS process. This process can also be conducted on inorganic substrates such as glass (Fig. S2). For inorganic substrates, an adhesive layer (such

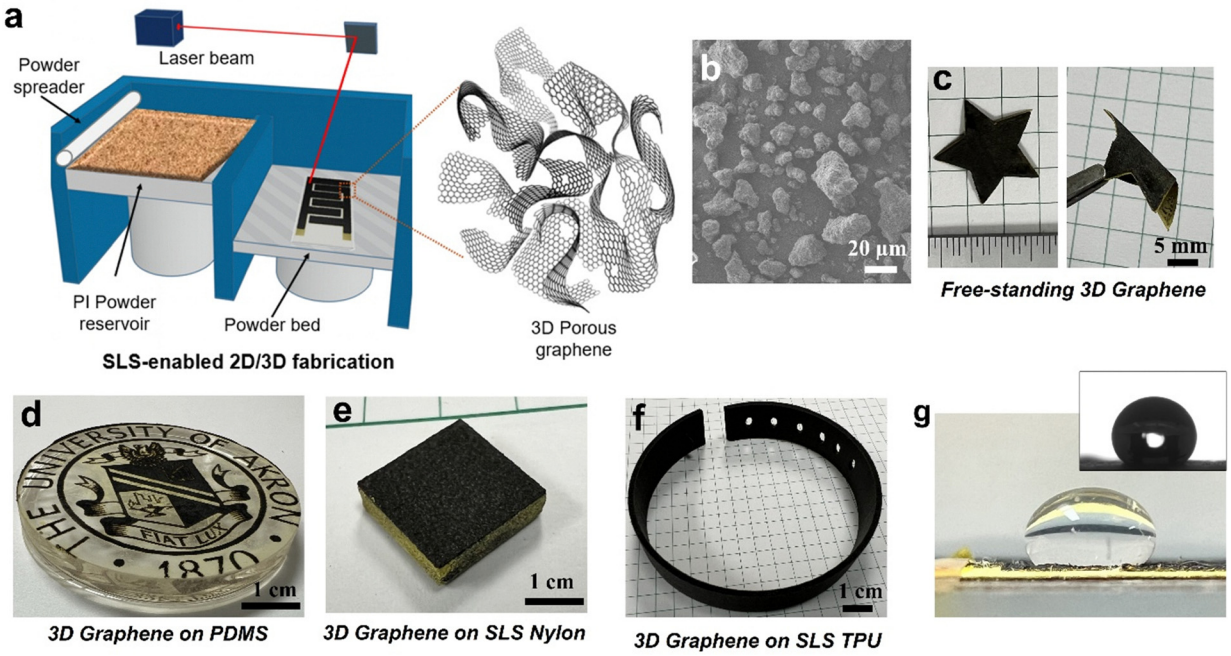

Fig. 1 (a) Schematic of the SLS-based fabrication of 3D graphene and hybrid structures. (b) SEM image of the PI microparticles. (c) Photos of a free-standing star-shaped porous graphene fabricated by the SLS with PI microparticles. (d) Photo of 3D patterned graphene in the shape of a university seal by SLS with PI microparticles on PDMS. (e) Photo of a 3D cuboid structure fabricated by sequential SLS with Nylon and PI microparticles. (f) Photo of a flexible wristband fabricated by sequential SLS with TPU and PI microparticles. (g) A drop of KOH solution on nanoporous graphene. Inset shows a water droplet on the 3D graphene during contact angle measurement.

as regular double-sided tape) is necessary to achieve sufficient adhesion of the fabricated 3D graphene structure to the substrates.

In the second approach, which is termed sequential SLS process, two types of polymer microparticles are used sequentially for SLS printing. The first SLS with polymer microparticles (such as Nylon or TPU) generates a 3D template or scaffold. Then the SLS-printed template is coated with PI microparticles and goes through the second SLS process to form a conductive graphene layer on its surface. Such sequential SLS is successfully demonstrated for the combination of Nylon and PI, as well as TPU and PI, which result in 3D graphene on Nylon and 3D graphene on TPU (Fig. 1e and f), respectively. In addition, due to the highly hydrophobic nature of graphene and the 3D porous morphology, the 3D graphene fabricated by SLS is expected to have interesting surface properties (Fig. 1g). We conducted contact angle measurements of the 3D graphene to different liquids, which shows a contact angle of $132 \pm 4.4^\circ$ to water and $142 \pm 3.2^\circ$ to glycerol. This also enables its potential applications in water repellent and hydrophobic coatings.

The structure of the 3D graphene formed by the SLS of PI microparticles is systematically investigated. SEM images (Fig. 2a and b) show that the formed 3D graphene has a hierarchical porous morphology with interconnected pores in the range of 1–5 μm (2.3 ± 0.7 μm in size for the pores visible from the top surface). Cross-section SEM image (Fig. 2c) further shows the internal structure of such 3D porous graphene. Such a morphology is analogous to 3D graphene foams which are usually fabricated by a CVD process with porous metal templates. Our process has the advantages of being template free and does not require gas precursors or direct heating to high temperatures. TEM image of the sample (Fig. 2d) shows the atomically thin structure with monolayer and multilayer of graphene.

We found that the cumulative laser irradiation intensity during the SLS process has a substantial effect on the 3D graphene formation. Because of the relatively low intensity (2.3 W) of the laser used in our SLS, one single scan at 50 mm s^{-1} on the PI microparticles is able to induce carbonization but not sufficient for high-quality graphene generation, this is shown by the Raman spectrum (Fig. 2e), which shows pronounced G band at 1585 cm^{-1} and D band at 1353 cm^{-1}, but with very low intensity 2D band, and the I_D/I_G ratio is 0.83. When the laser scanning is increased to two cycles, the 2D peaks intensity increases and the I_D/I_G ratio decreases to 0.77. When the laser scanning cycles increase to three, the 2D peak (at 2700 cm^{-1}) intensity is significantly higher, and the I_D/I_G ratio further decreases to 0.54.

The effects of laser scanning cycle on the structure and quality of the resulted 3D graphene are also reflected on their electrical conductivity. Representative *I–V* curves for the samples after 1, 2, and 3 cycles of SLS are shown in Fig. 2f. The sheet resistance decreases from 1166 Ω sq^{-1}, to 63 Ω sq^{-1}, and 21 Ω sq^{-1}, when the laser scanning cycle increases from one to three. XPS is also used to characterize the structure of the 3D graphene (Fig. 2g and h). Both C 1s and O 1s peaks are present,

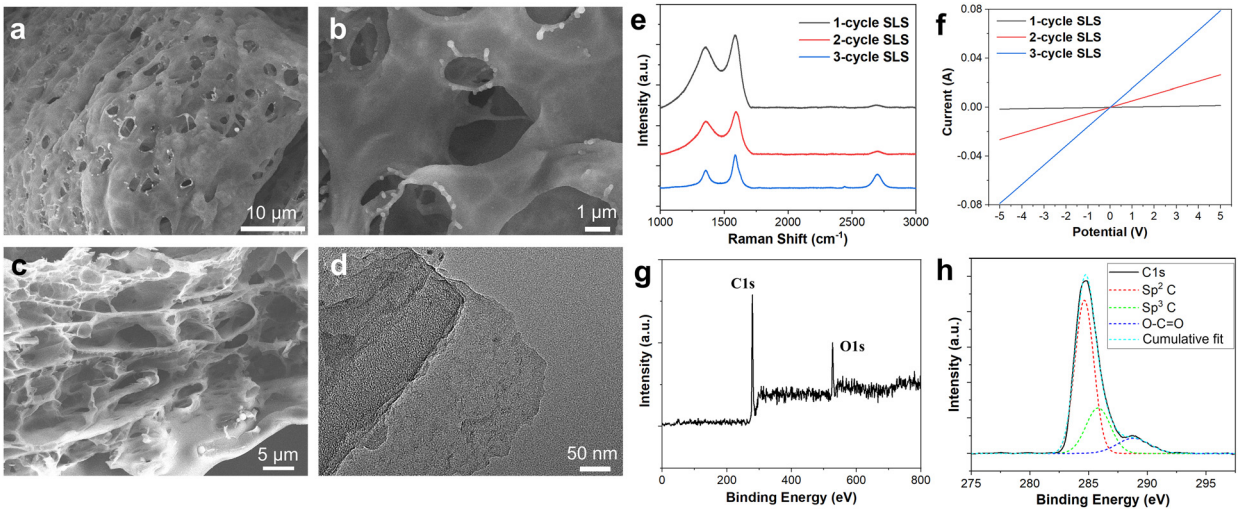

Fig. 2 (a) and (b) SEM images of the 3D graphene from SLS of PI microparticles. (c) Cross-section SEM image showing the porous internal structure. (d) TEM image of the obtained graphene structure. (e) Raman spectrum of the 3D graphene from SLS of PI microparticles with different laser scanning cycles. (f) *I*–*V* curves of the 3D graphene from SLS of PI microparticles with different laser scanning cycles. (g) XPS survey scan of the 3D graphene fabricated by SLS. (h) High-resolution XPS carbon peak and the peak fitting.

indicating the oxygen-containing groups exist on the 3D graphene. Deconvolution of the C 1s peak shows the main contribution is the sp^2 carbon peak at 284.5 eV, and minor peaks at 285.5 eV and 288.8 eV correspond to sp^3 carbon and O–C═O group, respectively. The main reason for the presence of oxygen-containing groups is the small extent of oxidation during the SLS process, which is conducted in air rather than inert gas environment.

We also conducted the control experiment using solid polyimide film as the precursor for LIG using the same laser scanning parameters as our SLS process. The results (Fig. S3) show that the graphene formed by laser scanning on solid PI film has a more open-pore structure with higher porosity and is substantially less conductive than the one formed by our SLS process with PI microparticles as the precursor. Raman spectrum of the control LIG sample (Fig. S4) shows an I_D/I_G ratio of 1.17, which is substantially higher than the 3D graphene formed from PI microparticle precursor (0.54). For further comparison (Table S2), the I_D/I_G ratio for conventional laser-induced graphene is in the range of 0.5 to 1.5, and most commonly in the range of 0.9–1.1,[27,42] due to the porous morphology, small graphitic domains, and abundant edges and vacancies.[47] The I_D/I_G ratio for CVD graphene foam is typically in the range of 0.7–1.3, and most commonly in the range of 0.8–1.0.[55,56]

To explain such differences, we conducted analytical modeling (details in the SI) of the local heat generation of the two systems: continuous PI film *vs.* monolayer of aggregated PI microparticles. For the case of PI microparticles, the small contact area between particles leads to low effective in-plane and through-plane conductivity, and the resulting poor heat spreading. Also, the areal heat capacity is also smaller than that of a continuous film due to voids and scattering. Both of which lead to higher local temperature increase and probably high graphitization extent, and the details can be found in the SI. Moreover, it is easier for the potential gas byproducts to release from powder precursors, so that fewer pores are formed on the surface.

2.2. Flexible supercapacitors based on SLS of PI microparticles

With the unique capability to fabricate patterned 3D graphene of precisely defined geometry and thickness, we utilized the SLS method to fabricate flexible supercapacitors. Supercapacitors are electrochemical energy storage devices with exceptional fast charging–discharging, long cycling stability.[57,58] In order to have sufficient surface area and electrical conductivity, it is desirable for the electrodes in supercapacitors to have tunable thickness,[59,60] this can be conveniently achieved by our SLS process.

SLS with one layer of PI microparticles (1-layer SLS) is able to generate well-defined 3D graphene pattern as the electrodes (Fig. 3a). To increase the thickness of the patterned electrodes, a fresh layer of PI microparticles can be coated on the fabricated structure, and SLS process is repeated to obtain a new layer of graphene with the exact same pattern that is strongly attached to the underlying graphene. Thus, 3D graphene-based interdigitated electrodes with various thicknesses can be obtained. Cross-section SEM images of such 3D graphene electrodes fabricated by different layers of SLS are shown in Fig. 3b–d. It can be seen that the 3D graphene has a porous morphology. The thickness increases from 45 μm for 1-layer SLS to around 100 μm and 140 μm for samples with 2-layer SLS and 3-layer SLS, respectively.

Flexible supercapacitors with interdigitated 3D graphene as the electrodes and PVA-H_2SO_4 as the gel electrolyte are fabricated, and their electrochemical performance is systematically investigated. Cyclic voltammetry (CV) results (Fig. 3e) show that quasi-rectangular shape without distinct peaks, indicative of

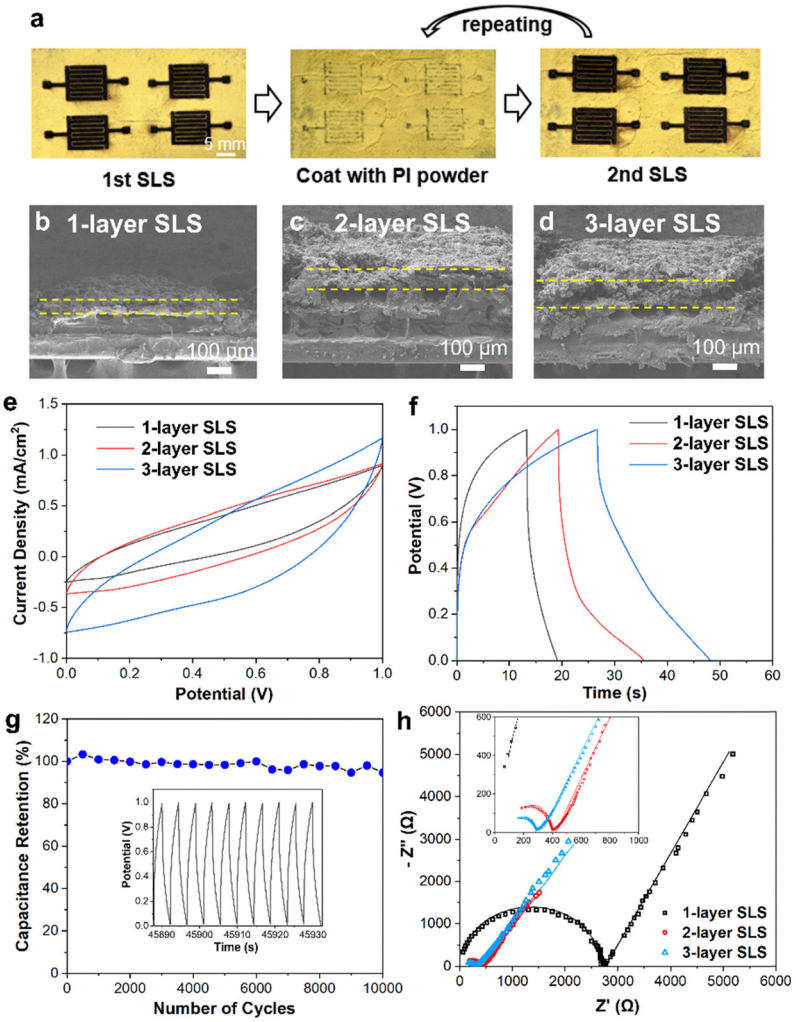

Fig. 3 (a) Photos of the SLS-based fabrication of supercapacitors with varying number of SLS graphene layers. (b)–(d) Cross-section SEM of the 3D graphene electrodes fabricated by SLS with different number of layers. (e) CV scan curves of the flexible supercapacitors fabricated by SLS of PI microparticles (scan rate: 50 mV s^{-1}). (f) GCV curves of the supercapacitors fabricated by SLS with different number of layers (measured at a current rate of 0.6 mA cm^{-2}) (g) Long-term stability testing of the supercapacitors as shown by the capacitance retention over 10 000 cycles, the inset shows the GCD curves of the last 10 cycles. (h) EIS curves of the supercapacitors fabricated by SLS with different number of layers. Inset shows the enlarged plots at the high-frequency region.

electrochemical double-layer capacitance (EDLC) behavior, which is typical for carbon-based electrodes. It is obvious that the enclosed area under the CV curves increased significantly with the number of SLS layers, suggesting enhanced energy storage capacity. The areal capacitance calculated from the CV testing at a scan rate of 50 mV s^{-1} is 5.9, 8.4, and 12.4 mF cm^{-2} for supercapacitors fabricated by 1-layer, 2-layer, and 3-layer SLS, respectively. This improvement with SLS layers is attributed to the increased 3D graphene volume and total surface area when the concurrent SLS and graphitization are repeated multiple times. The areal capacitance of such supercapacitors is also dependent on the scan rate (Fig. S5), and the capacitance increases with decreasing scan rate. For instance, the areal capacitance for 3-layer SLS sample increases to 45.4 mF cm^{-2} at 5 mV s^{-1} scan rate. This trend can be explained by the limited extent of ion diffusion at high scan rates, resulting in a reduction in charge storage capacity.

Galvanostatic charge–discharge (GCD) measurements were also conducted to evaluate the electrochemical performance of the SLS-fabricated supercapacitor. The devices were charged and discharged at a preset current density (range from 0.5 to 1.0 mA cm^{-2}) within the operational voltage window of 0 to 1 V (Fig. 3f). The GCD profiles have a quasi-triangle shape with rapid charge and discharge cycles, further confirming the EDLC character of the supercapacitors. Supercapacitors fabricated with higher number of SLS layers show longer charging and discharging duration, indicating an increase in energy storage capacity. GCD curves for those devices with varying current density are shown in Fig. S5. Higher current density leads to faster charging and discharging cycles.

To evaluate the long-term stability of the supercapacitor devices, we conducted long-term charge–discharge cycling test. For instance, the capacitance retention of supercapacitor fabricated by 3-layer SLS over 10 000 cycles (at a current density of

1 mA cm^{-2}) is shown in Fig. 3g. It can be seen that the capacitance remains stable with very small fluctuations, the retention rate is 94.7% of its initial value after 10 000 cycles, demonstrating the excellent stability of the supercapacitors fabricated by the concurrent SLS and graphitization method.

Electrochemical impedance spectrum (EIS) was carried out to further investigate the electrochemical responses and internal resistance of the supercapacitors. The Nyquist plots (the equivalent circuit for data fitting is included in Fig. S6) are shown in Fig. 3h. The high-frequency region (semicircle on the left) is related to the charge transfer resistance at the electrode/electrolyte interface and the low-frequency region (straight line on the right) indicates the ion diffusion behavior.[61] All three samples show characteristic 45° straight line in the low-frequency region, indicating the Warburg diffusion behavior typically observed in porous electrodes.[62,63] The charge transfer resistance (R_{ct}) obtained by fitting with the equivalent circuit model shows significant dependence on the number of SLS layers. The R_{ct} values decreases from 2578 Ω for 1-layer SLS, to 250 Ω and 144 Ω for 2-layer SLS and 3-layer SLS supercapacitor, respectively. The enhanced interfacial charge transfer efficiency with increasing SLS layers can be ascribed to the higher electrical conductivity and increased number of pores and microchannels inside the thicker 3D graphene electrodes.

2.3. 3D graphene-FeO_x hybrid structures based on SLS with hybrid PI microparticles

Our SLS-based 2D/3D fabrication approach is versatile with high tunability in terms of the chemical composition and physicochemical properties of the final structures. To demonstrate this, a convenient method to fabricate 3D graphene-FeO_x hybrids and supercapacitor devices is presented here. The main advantage of creating 3D graphene-FeO_x hybrids is that the additional component is electrochemically active and can further enhance the energy storage performance by adding pseudocapacitive property.

There are previous reports on combining conventional LIG with pseudocapacitive materials to enhance its energy storage performance, including the incorporation of heteroatom doping,[61,64] metal oxides,[36,38,65] conducting polymers.[66–68] However, balancing between structural integrity and energy storage capacity remains a challenge. The unique SLS process in our study is also very different from the doping/processing of conventional 2D LIG.

For our approach, in the first step, the PI microparticles are solution mixed with iron chloride ($FeCl_3$), which is adsorbed onto the surface of PI particles (Fig. S7). Then the modified PI microparticles are dried and dispersed into particle form again. TGA characterization (Fig. S8) of the PI and PI-$FeCl_3$ microparticles confirms the high thermal stability and the existence of both components. Such $FeCl_3$-modified PI particles are used for SLS fabrication following the same procedure as the pristine PI microparticles, except that two laser scanning speeds are tested: 50 mm s^{-1} (same as pristine PI) or 35 mm s^{-1}. The incorporation of $FeCl_3$ is also beneficial for the SLS process because it increases the laser absorption efficiency during SLS, and its catalytic activity also promotes graphene formation during the laser-induced carbonization.[4,5] During the SLS process, the $FeCl_3$ undergoes *in situ* oxidation and transforms into nanometer-sized iron oxide particles within the final 3D graphene structures.

The morphology of the 3D graphene-FeO_x hybrids is characterized by SEM and TEM (Fig. 4a and b). The overall structure is similar to the porous 3D graphene based on SLS with pristine PI microparticles, but with distinct nanoparticles decorated on graphene. TEM image shows the size of iron oxide

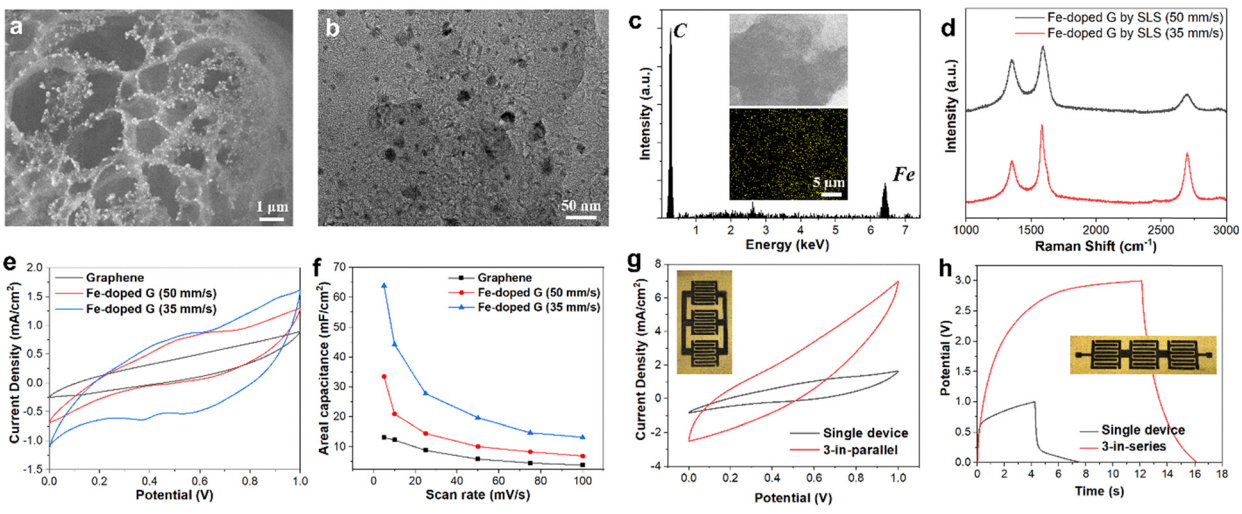

Fig. 4 (a) SEM and (b) TEM images of the hybrid 3D graphene-FeO_x fabricated by SLS. (c) EDX spectrum and Fe element mapping (inset) of the hybrid 3D graphene-FeO_x fabricated by SLS. (d) Raman spectra of the hybrid 3D graphene-FeO_x fabricated by SLS with two different laser scanning speeds. (e) CV curves (scan rate at 50 mV s^{-1}) of the flexible supercapacitor fabricated by SLS with hybrid 3D graphene-FeO_x or 3D graphene electrodes. (f) Comparison of the areal capacitance of the supercapacitor fabricated by SLS with hybrid 3D graphene-FeO_x (or 3D graphene as the control) electrodes. (g) Comparison of the CV curves for supercapacitors with hybrid 3D graphene-FeO_x electrode in single form or 3-in-parallel form. (h) Comparison of the GCD curves for supercapacitors with hybrid 3D graphene-FeO_x electrodes in single form or 3-in-series form.

nanoparticles is in the range of 5–15 nm. EDX spectrum (Fig. 4c) of the hybrid 3D graphene-FeO_x shows pronounced peaks for both carbon and iron. EDX mapping (Fig. 4c inset) shows that the iron element is uniformly distributed throughout the sample.

For the SLS-based fabrication of hybrid 3D graphene-FeO_x, because of the additional process of converting $FeCl_3$ into iron oxide NPs, it is beneficial to increase the laser irradiation time per unit area, which can be achieved by decreasing the laser scanning speed while using the same laser power. Therefore, we studied the effect of laser scanning speed by comparing a slower speed (35 mm s^{-1}) with the speed (50 mm s^{-1}) for SLS of pristine PI microparticles. Raman spectra of the hybrid 3D graphene-FeO_x fabricated by SLS with those two laser speeds are shown in Fig. 4d. It is obvious that the sample fabricated with the lower laser speed has a more pronounced 2D band. The I_D/I_G ratio also decreases from 0.84 to 0.61 for the two samples fabricated at 50 mm s^{-1} and 35 mm s^{-1}, respectively. This result indicates that slower laser scanning during SLS leads to higher quality hybrid 3D graphene-FeO_x that is less defective. The morphology of the hybrid 3D graphene-FeO_x shows higher porosity and thinner graphene shell when fabricated at lower laser scanning speed (Fig. S9). The electrical conductivity also shows an obvious increase with decreasing laser scanning speed (Fig. S10). The sheet resistance of hybrid 3D graphene-FeO_x fabricated at 50 mm s^{-1} and 35 mm s^{-1} to be 23.6 Ω sq^{-1} and 15.9 Ω sq^{-1}, respectively.

The hybrid 3D graphene-FeO_x is further used as the electrodes for supercapacitors. The representative CV curves for the hybrid 3D graphene-FeO_x supercapacitors and the control sample: pristine 3D graphene, are shown in Fig. 4e (also in Fig. S11). It can be seen that the enclosed area has a substantial increase for the hybrid 3D graphene-FeO_x compared with the undoped one, especially for the one fabricated at a lower laser speed. Moreover, for the hybrid 3D graphene-FeO_x sample fabricated at 35 mm s^{-1}, a pair of redox peaks: the oxidation peak at 0.56 V and the reduction peak at 0.36 V can be observed. Such redox peaks correspond to the valence state change of iron between Fe^{3+} and Fe^{2+}, and confirm the additional pseudocapacitive feature of the hybrid 3D graphene-FeO_x.

Such enhancement in energy storage capability is further characterized by GCD scans (Fig. S11). Compared with 3D graphene supercapacitors which show quasi-triangular charge–discharge profiles, the hybrid 3D graphene-FeO_x supercapacitors show substantially higher charging and discharging time, as well as plateaus at around the redox peak potential. EIS is also used to study the electrochemical properties of the supercapacitors (Fig. S12). Fitting of the EIS data with the equivalent circuit model shows that the charge transfer resistance is much smaller for the hybrid 3D graphene-FeO_x supercapacitors fabricated at lower laser speed, which is consistent with the higher electrical conductivity and porosity of the sample as discussed earlier.

The area capacitance calculated from the CV measurements are summarized in Fig. 4f. It can be seen that the hybrid 3D graphene-FeO_x supercapacitors have a much higher capacitance than the undoped counterpart. For instance, the area capacitance at a scan rate of 5 mV s^{-1} is 64.0 or 33.5 mF cm^{-2} for the hybrid 3D graphene-FeO_x supercapacitors fabricated at 35 mm s^{-1} or 50 mm s^{-1} laser speed, respectively, compared with 13.2 mF cm^{-2} for the undoped counterpart. The corresponding gravimetric capacitance of 3D graphene-FeO_x supercapacitor is about 470 F g^{-1}, and such performance is comparable or higher compared with energy storage devices based on conventional LIG (Table S3).

The main reason for such enhanced energy storage capability is ascribed to the addition of pseudocapacitive mechanism by iron oxide NPs, besides the EDLC behavior of the 3D graphene. Besides forming hybrids with iron oxide NPs, other types of metal oxide NPs in 3D graphene can also be conveniently achieved by our SLS process. For instance, when cobalt nitrate is integrated to the PI microparticles, the structures after SLS printing are hybrid 3D graphene-CoO_x and also show enhancement in its energy storage capability compared with undoped graphene (Fig. S13).

Furthermore, another advantage of our SLS-based fabrication strategy is the easy customization of the geometry and dimensions of the final products without the need for multi-step assembly. For instance, multiple interconnected supercapacitors in parallel or in series with hybrid 3D graphene-FeO_x as electrode can be conveniently fabricated by one SLS process. For the 3-in-parallel device (Fig. 4g), the current density is significantly increased at the same voltage window, and the GCD curve shows nearly tripled discharging time (Fig. S14). For the 3-in-series device, the potential window triples, reaching 0–3 V in both the CV and GCD testing, while maintaining a similar discharge time. To showcase practical applications, we used the 3-in-series supercapacitor to power up a red LED device as well as a laboratory timer (Fig. S14).

2.4. Sequential SLS with multiple types of microparticles for hybrid 3D functional structures

Beyond SLS with PI microparticles for the fabrication of porous 3D graphene and functional devices, our approach also enables sequential SLS with two types of polymer microparticles for the fabrication of hybrid 3D functional structures (Fig. 5a). Specifically, the first SLS process is conducted with conventional polymer particles for the fabrication of a 3D template. Then, the 3D template is coated with PI microparticles, and the second SLS process is conducted. This enables the direct fabrication of 3D hierarchical structures with a conductive graphene surface in the same fabrication platform, which is superior to conventional approaches that require separate graphene fabrication and transfer.[69–72]

In our study, we conducted the first SLS with TPU microparticles (Fig. S15) to create a soft and flexible template. Then, the TPU 3D structures were coated with PI microparticles and used for the second SLS process to convert the PI into 3D porous graphene *in situ*. Representative 3D structures with 3D porous graphene on 3D TPU templates such as a wristband and rings are shown in Fig. 5b and c. Raman spectrum of such 3D hybrid graphene-TPU structure shows strong G, D, and 2D

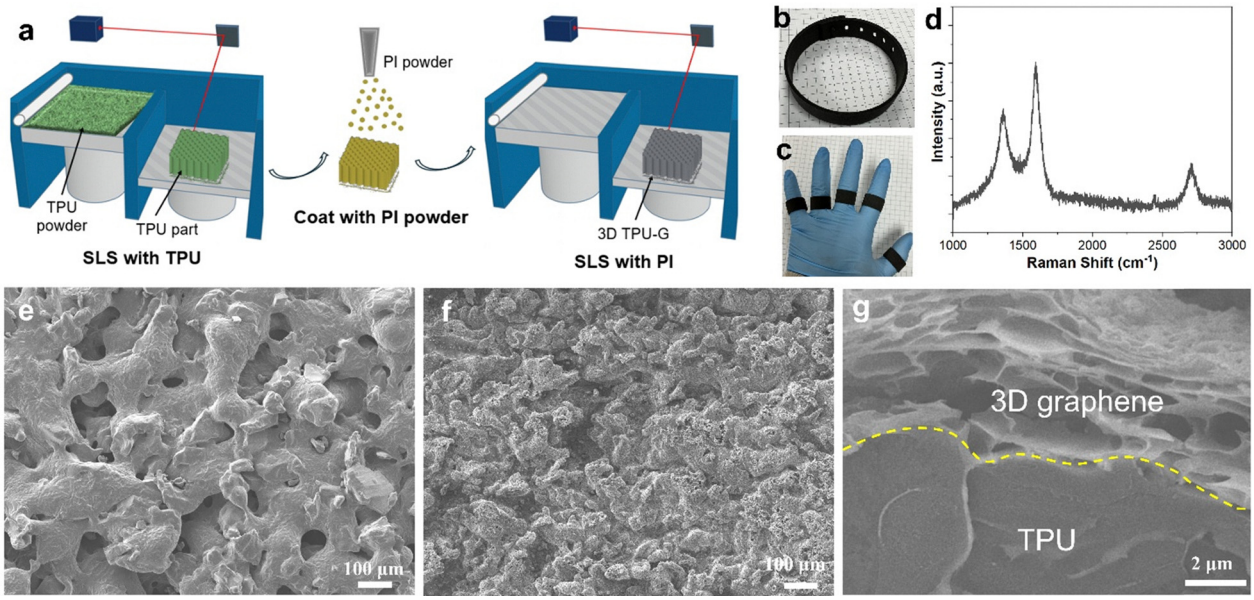

Fig. 5 (a) Scheme of the integrated SLS process for the fabrication of soft and conductive 3D TPU-graphene structures. (b) and (c) Photos of the SLS-printed wearable wristband and rings. (d) Raman spectrum of the SLS-printed 3D TPU-graphene structure. (e) SEM of the surface of as-fabricated 3D TPU. (f) SEM of the surface of the SLS-printed 3D TPU-graphene structure. (g) Cross-section SEM of the SLS-printed 3D TPU-graphene structure.

bands, with an I_D/I_G ratio of 0.65, indicating 3D graphene coating is generated.

The 3D TPU template fabricated after the first SLS (Fig. 5e) shows a rough surface due to the incomplete coalescence of TPU microparticles at the surface. This is beneficial for its strong adhesion to PI microparticles in the following step. After the second SLS process with coated PI microparticles on the surface, the surface shows a porous 3D graphene morphology. Cross-section SEM of the fabricated 3D hybrid graphene-TPU (Fig. 5g) shows clearly the porous graphene on top of a dense TPU template. The strong bonding between the graphene layer and TPU template can be observed, which can be explained by the laser irradiation during the second SLS process of PI microparticles also partially melts the underlying TPU surface layer, which can diffuse and form tight bonding with the bottom surface of the porous graphene layer. The SLS-printed TPU supporting part has a uniform structure with a small extent of porosity (Fig. S16). We also studied the mechanical response of the SLS-printed TPU under cyclic tensile stress (Fig. S17), which shows softening or decrease in modulus after the first loading-unloading cycle due to the Mullins effect,[73] but maintains stable and fully reversible the subsequent cycles.

The 3D hybrid graphene-TPU structures fabricated by the sequential SLS process are ideal platform for flexible electronics and sensors due to their high stretchability and tunable conductivity. To demonstrate this, we fabricated rectangular bars of such 3D hybrid graphene-TPU and studied their electrical responses against mechanical stretching. Fig. 6a shows the relative resistance against repeated stretching (to 3% strain) and relaxation cycles at various frequencies. It can be seen that the electrical responses are rapid and highly reproducible, especially at high frequencies. The magnitude of such relative resistance is strongly dependent on the strain or extent of deformation (Fig. 6b). The R/R_0 ratio increases from 2.2 to 3.0 when the maximum strain during the cyclic stretching increases from 5% to 10%. The long-term performance of such flexible strain sensors is also studied (Fig. 6c). The device shows excellent stability after 10 000 cycles at 10% maximum strain with very small fluctuations in its relative resistance values.

Furthermore, it is discovered that the SLS fabrication process has substantial effects on the electrical responses of such 3D hybrid graphene-TPU as strain sensors (Fig. 6d). The above discussed data are based on devices fabricated with laser scanning direction along the transverse direction or at 90° of the long axis (stretching direction). We also fabricated 3D hybrid graphene-TPU with the exact same geometry and composition but with laser scanning along the longitudinal direction or at 0° of the long axis.

The relative resistance change as a function of strain of those two types of strain sensors are shown in Fig. 6e and f. Both type of sensors show increased electrical response with larger strain. Such increase is nonlinear or with multi-stage electrical responses. From the slope of such curve, the Gauge factor (GF), which is the ratio of relative resistance change to strain, can be calculated. The strain sensor fabricated with 90° laser scanning direction shows a GF of 3.6 at 5% strain or lower, which increases to 26 between 5% to 17% strain, and further to 95 between 17% to 27% strain. On the other hand, the hybrid graphene-TPU sensor fabricated with 0° laser scanning direction shows a much higher GF: reaching 128 between 8% and 18% strain, and 680 between 18% to 23% strain. Moreover, the 0° laser scanning sample shows an abrupt drop in conductivity after 23% strain, indicating macroscopic crack or fracture of the graphene layer at this stage. We compared the strain sensor

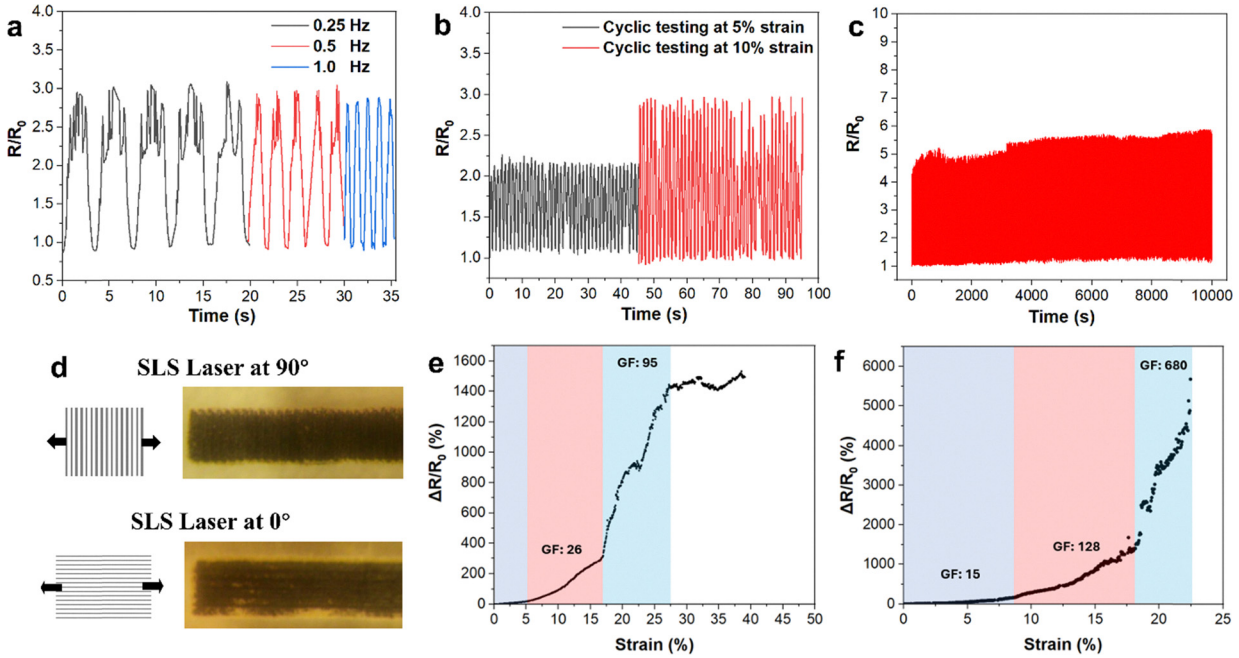

Fig. 6 (a) Relative resistance changes during cyclic tensile strain (to 3%) at three different frequencies. (b) Relative resistance changes during cyclic tensile testing (at 1 Hz frequency) with two different maximum strains. (c) Long-term electrical responses to cyclic tensile strain (10% strain and 1 Hz frequency) up to 10 000 cycles. (d) Scheme and photo of the SLS-printed 3D TPU-graphene structures with laser scanning directions along the transverse (90°) and longitudinal (0°) of the sample. (e and f) Relative resistance change as a function of tensile strain for the SLS-printed 3D TPU-graphene with laser scanning along (e) transverse direction and (f) longitudinal direction.

performance with relevant literature reports (Table S4), especially those based on LIG, and our system shows advantages in high gauge factor and detection range.

The main reason for such a pronounced difference in the electrical responses of the hybrid graphene-TPU sensor fabricated by 90° and 0° laser scanning directions can be explained by the interfacial structure of the 3D graphene. During the SLS process, the interface regions between the neighboring laser scanning pathways experience lower laser irradiation intensity, thus having lower quality graphene or a larger extent of amorphous structures, which is also more flexible and stretchable compared with the higher quality graphene within the laser scanning path. Therefore, when the stretching direction is along the transverse direction, such interfacial regions are deformed more readily, leading to smaller changes to the overall resistance and higher strain at break. When the stretching direction is along the longitudinal direction, the deformation is directly on the higher quality 3D graphene rather than the interfacial region, which results in lower stretchability but greater change in the electrical resistance. Such unique properties of the SLS-fabricated hybrid strain sensors provide a versatile platform for wearable and stretchable electronics and sensing.

The SLS-based fabrication approach demonstrated in this work has several advantages compared with conventional device fabrication methods. Unlike lithography-based microfabrication or screen-printing techniques that require multiple processing steps, the present method utilizes direct laser conversion of a coated polyimide precursor, enabling mask-free, programmable patterning of conductive graphene structures. Because the precursor can be applied as a coating layer, the process can be readily implemented on various substrate geometries and surfaces, including planar, curved, and flexible platforms. This versatility makes the approach particularly attractive for rapid prototyping and scalable manufacturing of flexible sensors and integrated energy storage devices. Moreover, the capability to directly pattern both sensing component and energy-storage unit using the same laser writing process provides a potential pathway for integrated fabrication of multifunctional devices.

3. Conclusion

To sum up, in this study we successfully demonstrated a new approach for the precise manufacturing of 2D/3D conductive and flexible structures for energy storage and sensing. Our approach is based on selective laser sintering with PI or its hybrid microparticles, which have the unique capability of concurrent sintering and graphitization. Moreover, by sequential SLS with two types of polymer particles, conductive graphene-coated 3D polymeric structures can be conveniently fabricated, which show great potential as soft and stretchable strain sensors.

Concurrent SLS and graphitization of PI microparticles on flexible substrates enable the fabrication of supercapacitors with excellent and tunable energy storage capacity. It is found that the laser scanning cycle and thickness/number of layers of

the 3D graphene electrodes have significant effects on the capacity. Moreover, by incorporating iron chloride with PI microparticles during SLS, hybrid 3D graphene-FeO_x supercapacitors can be fabricated, which shows 3–5 folds increases in energy storage capacity compared with the undoped counterparts. Sequential SLS with TPU and PI microparticles enables the fabrication of flexible strain sensors that have high sensitivity with gauge factor as high as 680, and excellent long-term stability over 10 000 cycles. In addition, we find that the laser scanning direction during the SLS fabrication (transverse or longitudinal of the long axis) has substantial effects on the electrical responses during mechanical deformation. Our approach uniquely combines the advantages of SLS 3D printing with structural transformation of polymer microparticles provides a versatile platform for the advanced manufacturing of functional devices for energy storage and flexible electronics.

4. Experimental section

4.1. Materials and equipment

Polyimide powder (AURUM TPI) was provided by Mitsui Chemicals, Polyvinyl alcohol (PVA), potassium hydroxide (KOH), and iron chloride ($FeCl_3{\cdot}6H_2O$) were purchased from Sigma Aldrich. The SLS printing was conducted with a desktop 3D printer (Sintratec Kit) equipped with a diode laser (wavelength of 455 nm and power of 2.3 W).

4.2. SLS with PI microparticles on various substrates

PI microparticles were ground using a pestle and mortar to break down any aggregations. For SLS of PI microparticles on polymer substrates, including PET and PDMS, the substrates were dipped into a reservoir of PI particles, and the electrostatic attraction led to a uniform layer of PI particles attached to the substrate. The average areal density of the PI particles on polymer substrates was measured to be 1.58 ± 0.18 mg cm^{-2}. For SLS of PI microparticles on inorganic substrates such as glass and steel, an adhesive layer (regular double-sided tape) was first applied to the substrates, and then PI particles were spread onto the surface with a blade coater. The average areal density of the PI particles on inorganic substrates was measured to be 1.11 ± 0.16 mg cm^{-2}. The SLS of PI particles was then conducted with the SLS printer following different protocols based on the final applications, as described below.

4.3. Flexible supercapacitors based on SLS of PI microparticles

The flexible supercapacitors were fabricated by SLS of PI microparticles on a PET substrate (PET is just a supporting substrate and not involved in the SLS process). The interdigitated electrodes are composed of four fingers on each side, each finger is 9 mm in length and 1 mm in width, with a 0.25 mm gap between the opposite electrode fingers. The laser scanning speed was fixed at 50 mm s^{-1}, the hatch spacing was set at 125 μm, and laser sintering of the electrode patterns was repeated three times.

To fabricate supercapacitors with thicker electrodes, the PI microparticles deposition and SLS can be repeated two or three times over the same pattern. After SLS process of each layer, the patterns were washed with DI water and ethanol to remove excessive PI particles between electrode fingers.

The gel electrolyte was prepared by dissolving 1 g KOH in 5 mL DI water and 1 g PVA in 10 mL DI water and mixing them well. The gel electrolyte was then evenly spread on the surface of the graphitized electrodes. The supercapacitor assembly was completed by connecting the electrodes with thin copper foil using silver paste for electrical contact.

Furthermore, to fabricate flexible supercapacitors with hybrid 3D graphene-FeO_x electrode, the PI microparticles were first thoroughly mixed with $FeCl_3{\cdot}6H_2O$ at a weight ratio of 5 : 1 in ethanol. Then the mixed particles were dried at 80 °C and ground into fine powders using an IKA high-speed analytical mill. The fabrication of hybrid 3D graphene-FeO_x electrodes with the mixed powders was conducted using the same SLS process as described above, except that the laser scanning speed was 50 or 35 mm s^{-1}. The gel electrolyte and final supercapacitor assembly were also conducted by the same procedure.

4.4. Soft and stretchable sensors based on integrated SLS

The soft strain sensor was fabricated by sequential SLS with two types of microparticles: TPU and PI. SLS with TPU microparticles (Sintratec TPE) was conducted first to fabricate the flexible base layer with a thickness of about 1 mm. Then, PI microparticles were spread on the surface of the SLS-printed TPU layer, and SLS process of PI was conducted following the same procedure as described earlier. The mechanical stretching of such TPU-3D graphene strain sensor was conducted with an automated uniaxial moving stage. Electrical signal recording was conducted with a Keithley 2400 multimeter.

4.5. Characterization

SEM was conducted with a JEOL-7401 FE-SEM operating at 5.0 kV with an 8 mm working distance. TEM was conducted with a FEI Tecnai F20. Raman Spectroscopy was carried out using a Horiba LabRAM HR800 confocal Raman. X-ray photoelectron spectroscopy (XPS) was performed using the PHI 5000 Versaprobe II system. *I–V* curves were obtained using a Keithley 2400 through a two-point connection with fixed geometry of the samples (2 cm × 1 cm).

Electrochemical measurements were conducted in a 2-electrode configuration. Cyclic voltammetry (CV) and Galvanostatic charge and discharge (GCD) measurements were carried out using a CHI 660D electrochemical workstation. CV was measured at different scan rates ranging from 5 mV s^{-1} to 100 mV s^{-1}. GCD was measured at different current densities from 1 to 10 mA cm^{-2}. Electrochemical impedance spectroscopy (EIS) was recorded using a HP 4192A LF Impedance Analyzer at a frequency range of 5 Hz to 13 MHz.

Author contributions

W. X. designed and supervised the research. M. Y. conducted most of the experiments and data analysis. J. B. conducted the electron microscopy experiments. P. N. D, L. D., M. L., and L. B. contributed to the experiments. M. Y. and W. X. wrote the original manuscript. All authors reviewed and approved the final manuscript.

Conflicts of interest

The authors declare no conflict of interest.

Data availability

The data supporting this article have been included as part of the supplementary information (SI). Supplementary information: Fig. S1 to S10, and further experimental details. See DOI: https://doi.org/10.1039/d6mh00119j.

Acknowledgements

W. X. gratefully acknowledges the support of the ACS PRF New Direction grant (No. 67730-ND7). We would also like to thank Mitsui Chemicals for the PI samples.

References

1 A. Kamyshny and S. Magdassi, *Chem. Soc. Rev.*, 2019, **48**, 1712.
2 R. Bo, S. Xu, Y. Yang and Y. Zhang, *Chem. Rev.*, 2023, **123**, 11137.
3 J. Zhao, H. Yi, M. Xu, S. Wang, L. Fan, Y. Ma, Z. Yang and Z. Li, *Adv. Mater.*, 2025, e10294.
4 R. Krishnamoorti and R. A. Vaia, *J. Polym. Sci., Part B: Polym. Phys.*, 2007, **45**, 3252.
5 A. D. Valino, J. R. C. Dizon, A. H. Espera, Q. Chen, J. Messman and R. C. Advincula, *Prog. Polym. Sci.*, 2019, **98**, 101162.
6 J. Huang, J. Zhou and M. Liu, *JACS Au*, 2022, **2**, 280.
7 M. Yang, M. Guo, E. Xu, W. Ren, D. Wang, S. Li, S. Zhang, C.-W. Nan and Y. Shen, *Nat. Nanotechnol.*, 2024, **19**, 588.
8 W. H.-Y. Clarissa, C. H. Chia, S. Zakaria and Y. C.-Y. Evyan, *Prog. Addit. Manuf.*, 2022, **7**, 325.
9 J. R. Tumbleston, D. Shirvanyants, N. Ermoshkin, R. Janusziewicz, A. R. Johnson, D. Kelly, K. Chen, R. Pinschmidt, J. P. Rolland, A. Ermoshkin, E. T. Samulski and J. M. DeSimone, *Science*, 2015, **347**, 1349.
10 R. L. Truby and J. A. Lewis, *Nature*, 2016, **540**, 371.
11 N. Shen, S. Liu, P. Kasbe, F. Khabaz, J. P. Kennedy and W. Xu, *ACS Appl. Polym. Mater.*, 2021, **3**, 4554.
12 N. Shen, L. Duan, M. Yang, S. Liu and W. Xu, *MRS Commun.*, 2022, **12**, 597.
13 S. Liu, M. Yang, H. Barton and W. Xu, *ACS Appl. Mater. Interfaces*, 2024, **16**, 5513.
14 M. Schmid, A. Amado and K. Wegener, *J. Mater. Res.*, 2014, **29**, 1824.
15 M. S. Hassan, K. M. M. Billah, S. E. Hall, S. Sepulveda, J. E. Regis, C. Marquez, S. Cordova, J. Whitaker, T. Robison, J. Keating, E. Shafirovich and Y. Lin, *J. Compos. Sci.*, 2022, **6**, 41.
16 D. Ruggi, M. Lupo, D. Sofia, C. Barrès, D. Barletta and M. Poletto, *Powder Technol.*, 2020, **370**, 288.
17 J. Kruth, P. Mercelis, J. Van Vaerenbergh, L. Froyen and M. Rombouts, *Rapid Prototyp. J*, 2005, **11**, 26.
18 X. Li, H. Ouyang, S. Sun, J. Wang, G. Fei and H. Xia, *ACS Appl. Polym. Mater.*, 2023, **5**, 2944.
19 B. Li, W. Liang, F. Ren and F. Xuan, *Mater. Lett.*, 2022, **324**, 132764.
20 X. Yang, Y. Wei, S. Xi, Y. Huang, M. Kong and G. Li, *Polymer*, 2019, **172**, 58.
21 X. Wang, Z. Wang, S. Xiang, M. Peng, G. Li and Y. Huang, *Addit. Manuf.*, 2024, **86**, 104188.
22 Y. Zhou, S. Xi, Y. Huang, M. Kong, Q. Yang and G. Li, *Mater. Des.*, 2020, **190**, 108578.
23 M. Yang, J. Bu, N. Shen, S. Liu and W. Xu, *Adv. Mater. Technol.*, 2024, 2400890.
24 A. Griffin, M. Yang, P. Frame, W. Xu and Z. Qiang, *ACS Appl. Eng. Mater.*, 2025, **3**, 2391.
25 W. Han, L. Kong and M. Xu, *Int. J. Extreme Manuf.*, 2022, **4**, 042002.
26 X. Gan, G. Fei, J. Wang, Z. Wang, M. Lavorgna and H. Xia, *In Structure and Properties of Additive Manufactured Polymer Components*, Elsevier, 2020, pp. 149–185.
27 J. Lin, Z. Peng, Y. Liu, F. Ruiz-Zepeda, R. Ye, E. L. G. Samuel, M. J. Yacaman, B. I. Yakobson and J. M. Tour, *Nat. Commun.*, 2014, **5**, 5714.
28 F. Mahmood, H. Zhang, J. Lin and C. Wan, *ACS Omega*, 2020, **5**, 14611.
29 H. Wang, H. Wang, Y. Wang, X. Su, C. Wang, M. Zhang, M. Jian, K. Xia, X. Liang, H. Lu, S. Li and Y. Zhang, *ACS Nano*, 2020, **14**, 3219.
30 Y. Chyan, R. Ye, Y. Li, S. P. Singh, C. J. Arnusch and J. M. Tour, *ACS Nano*, 2018, **12**, 2176.
31 R. Ye, Y. Chyan, J. Zhang, Y. Li, X. Han, C. Kittrell and J. M. Tour, *Adv. Mater.*, 2017, **29**, 1702211.
32 A. C. Bressi, A. Dallinger, Y. Steksova and F. Greco, *ACS Appl. Mater. Interfaces*, 2023, **15**, 35788.
33 Y. Xu, Q. Fei, M. Page, G. Zhao, Y. Ling, D. Chen and Z. Yan, *Nano Res.*, 2021, **14**, 3033.
34 Y. Ling, W. Pang, X. Li, S. Goswami, Z. Xu, D. Stroman, Y. Liu, Q. Fei, Y. Xu, G. Zhao, B. Sun, J. Xie, G. Huang, Y. Zhang and Z. Yan, *Adv. Mater.*, 2020, **32**, 1908475.
35 A. Dallinger, P. Kindlhofer, F. Greco and A. M. Coclite, *ACS Appl. Polym. Mater.*, 2021, **3**, 1809.
36 S. Remesh, N. N. Loganathan, V. Perumal, M. Ovinis, S. Karuppanan, T. N. J. I. Edison, P. B. Raja, M. N. M. Ibrahim, N. Arumugam and R. S. Kumar, *J. Energy Storage*, 2024, **77**, 109920.
37 G. Yuan, T. Wan, A. BaQais, Y. Mu, D. Cui, M. A. Amin, X. Li, B. B. Xu, X. Zhu, H. Algadi, H. Li, P. Wasnik, N. Lu, Z. Guo, H. Wei and B. Cheng, *Carbon*, 2023, **212**, 118101.

38 M. Reina, M. Serrapede, P. Zaccagnini, A. Pedico, M. Castellino, S. Bianco, T. Ouisse, H. Pazniak, J. Gonzalez-Julian and A. Lamberti, *Electrochim. Acta*, 2023, **468**, 143163.
39 M. Hu, P. He, W. Zhao, X. Zeng, J. He, Y. Chen, X. Xu, J. Sun, Z. Li and J. Yang, *ACS Appl. Mater. Interfaces*, 2023, **15**, 51360.
40 A. Chhetry, Md Sharifuzzaman, H. Yoon, S. Sharma, X. Xuan and J. Y. Park, *ACS Appl. Mater. Interfaces*, 2019, **11**, 22531.
41 H. Wang, Z. Zhao, P. Liu, Y. Pan and X. Guo, *ACS Appl. Mater. Interfaces*, 2022, **14**, 41283.
42 R. Ye, D. K. James and J. M. Tour, *Acc. Chem. Res.*, 2018, **51**, 1609.
43 Y. Lu, Z. Jin, Q. Sheng, D. Kong, C. Miao, H. Wu, G. Pang, H. Xie, L. Xie, G. Yang, J. Zou, H. Yang, W. Huang and K. Xu, *Nat. Commun.*, 2026, **17**, 1381.
44 L. Zheng, Y. Lu, H. Lyu, T. Li, S. Cui, Y. Xu, Z. Cai, Y. Hou, Y. Li, Q. Yang, Z. Ye, G. Yang and K. Xu, *Biosens. Bioelectron.*, 2026, **298**, 118386.
45 S. A. A. Shah, R. Idrees and S. Saeed, *J. Energy Storage*, 2022, **55**, 105667.
46 T.-S. D. Le, H.-P. Phan, S. Kwon, S. Park, Y. Jung, J. Min, B. J. Chun, H. Yoon, S. H. Ko, S.-W. Kim and Y.-J. Kim, *Adv. Funct. Mater.*, 2022, **32**, 2205158.
47 R. Ye, D. K. James and J. M. Tour, *Adv. Mater.*, 2019, **31**, 1803621.
48 E. Joanni, R. Kumar, W. P. Fernandes, R. Savu and A. Matsuda, *Nanoscale*, 2022, **14**, 8914.
49 A. P. Tiwari, G. Bae, Y. Yoon, K. Kim, J. Kim, Y.-L. Lee, K.-S. An and S. Jeon, *ACS Sustainable Chem. Eng.*, 2023, **11**, 5229.
50 A. P. Tiwari, J. E. Patterson, M. S. Rahman and W. J. Scheideler, *Adv. Mater. Technol.*, 2025, **10**, e00122.
51 G. Antonelli, G. Curci, J. Filippi, A. Bernardini, M. Menegazzo, M. Marini, A. Agresti, S. Pescetelli, V. Lacconi, M. Massimiani, M. D'Orazio, P. Casti, L. Campagnolo, G. Bussetti, A. Mencattini and E. Martinelli, *Sens. Actuators, A*, 2024, **377**, 115746.
52 A. Lamberti, F. Clerici, M. Fontana and L. Scaltrito, *Adv. Energy Mater.*, 2016, **6**, 1600050.
53 B. Sun, R. N. McCay, S. Goswami, Y. Xu, C. Zhang, Y. Ling, J. Lin and Z. Yan, *Adv. Mater.*, 2018, **30**, 1804327.
54 H. Hatori, Y. Yamada, M. Shiraishi, M. Yoshihara and T. Kimura, *Carbon*, 1996, **34**, 201.
55 J. Jia, X. Sun, X. Lin, X. Shen, Y.-W. Mai and J.-K. Kim, *ACS Nano*, 2014, **8**, 5774.
56 M. Huang, C. Wang, L. Quan, T. H.-Y. Nguyen, H. Zhang, Y. Jiang, G. Byun and R. S. Ruoff, *Matter*, 2020, **3**, 487.
57 Q. Zhu, D. Zhao, M. Cheng, J. Zhou, K. A. Owusu, L. Mai and Y. Yu, *Adv. Energy Mater.*, 2019, **9**, 1901081.
58 Y. Shao, M. F. El-Kady, J. Sun, Y. Li, Q. Zhang, M. Zhu, H. Wang, B. Dunn and R. B. Kaner, *Chem. Rev.*, 2018, **118**, 9233.
59 M. Yang, P. Kasbe, J. Bu and W. Xu, *Nanoscale*, 2024, **16**, 8390.
60 M. Yang, Y. Liu, X. Luo, Y. Cao, X. Gong and W. Xu, *ACS Appl. Energy Mater.*, 2021, **4**, 10069.
61 M. Khandelwal, C. V. Tran, J. Lee and J. B. In, *Chem. Eng. J.*, 2022, **428**, 131119.
62 M. Yuan, F. Luo, Z. Wang, H. Li, Y. Rao, J. Yu, Y. Wang, D. Xie, X. Chen and C.-P. Wong, *ACS Appl. Mater. Interfaces*, 2021, **13**, 22426.
63 T. S. Mathis, N. Kurra, X. Wang, D. Pinto, P. Simon and Y. Gogotsi, *Adv. Energy Mater.*, 2019, **9**, 1902007.
64 Z. Peng, R. Ye, J. A. Mann, D. Zakhidov, Y. Li, P. R. Smalley, J. Lin and J. M. Tour, *ACS Nano*, 2015, **9**, 5868.
65 R. Ye, Z. Peng, T. Wang, Y. Xu, J. Zhang, Y. Li, L. G. Nilewski, J. Lin and J. M. Tour, *ACS Nano*, 2015, **9**, 9244.
66 F. Tehrani, M. Beltrán-Gastélum, K. Sheth, A. Karajic, L. Yin, R. Kumar, F. Soto, J. Kim, J. Wang, S. Barton, M. Mueller and J. Wang, *Adv. Mater. Technol.*, 2019, **4**, 1900162.
67 A. Khodabandehlo, A. Noori, M. S. Rahmanifar, M. F. El-Kady, R. B. Kaner and M. F. Mousavi, *Adv. Funct. Mater.*, 2022, **32**, 2204555.
68 A. Ladrón-de-Guevara, A. Boscá, J. Pedrós, E. Climent-Pascual, A. de Andrés, F. Calle and J. Martínez, *Appl. Surf. Sci.*, 2019, **467–468**, 691.
69 H. Liu, H. Xiang, Z. Li, Q. Meng, P. Li, Y. Ma, H. Zhou and W. Huang, *ACS Sustainable Chem. Eng.*, 2020, **8**, 527.
70 T. Pinheiro, R. Correia, M. Morais, J. Coelho, E. Fortunato, M. G. F. Sales, A. C. Marques and R. Martins, *ACS Nano*, 2022, **16**, 20633.
71 W. Wang, L. Lu, Z. Li, L. Lin, Z. Liang, X. Lu and Y. Xie, *ACS Appl. Mater. Interfaces*, 2022, **14**, 1315.
72 Y. Lu, G. Yang, S. Wang, Y. Zhang, Y. Jian, L. He, T. Yu, H. Luo, D. Kong, Y. Xianyu, B. Liang, T. Liu, X. Ouyang, J. Yu, X. Hu, H. Yang, Z. Gu, W. Huang and K. Xu, *Nat. Electron.*, 2023, **7**, 51.
73 X. Liu, N. Shen, J. Bu, M. Yang, X. Guan and W. Xu, *J. Mater. Chem. A*, 2025, **13**, 32134.

